

## Manuscript Supplement

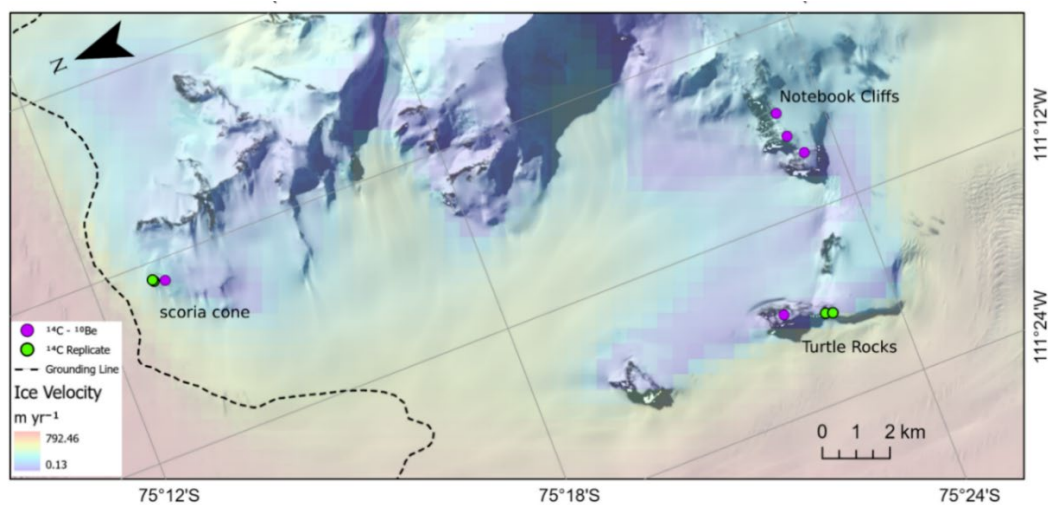
This supplement provides additional context for the main paper and is divided into the following sections:

**S1** - Geomorphic Context, **S2** - Comparison of excess scatter of in situ  $^{14}\text{C}$  and  $^{10}\text{Be}$  data from Mt Murphy

- 5 **S3** - Assessment of Mt Murphy quartz separates impact on in situ  $^{14}\text{C}$  reproducibility and **S4** - Holocene filter age vs elevation plots and paired nuclide diagrams.

### **Supplement S1: Geomorphic Context**

- 10 Here, we detail the geomorphic context for each sample at Mt Murphy for which a paired  $^{14}\text{C}$ - $^{10}\text{Be}$  nuclide measurement has been performed. A full site description of scoria cone can be found in Adams et al., (2022). A site description of both Turtle Rock and Notebook Cliffs can be found in Johnson et al., (2020).



- 15 **Figure S1.** Mt Murphy sites and locations measured for both in situ  $^{14}\text{C}$  and  $^{10}\text{Be}$  displayed in the context of local ice velocities. Landsat-9 image from the online Data Pool, courtesy of the NASA EOSDIS Land Processes Distributed Active Archive Center (LP DAAC). Ice flow speeds are overlain to improve visualisation of ice localised ice flow and were downloaded from MEaSUREs InSAR-Based Antarctica Ice Velocity Dataset Version 2 (Mouginot et al., 2012, 2017; Rignot et al., 2011) (Mouginot et al., 2012, 2017; Rignot et al., 2011b) [last accessed 25.05.2023]. Grounding line from (Milillo et al., 2022).

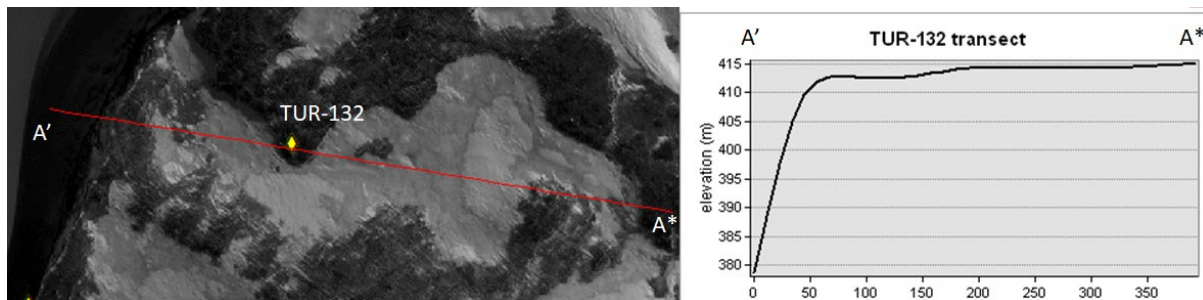
### 20 **TURTLE ROCK**

Many erratic boulders and cobbles have been recovered from Turtle Rock (Johnson et al., 2020). The lowest terrace from where TUR-117 and TUR-132 were recovered is relatively flat and also hosts the greatest density of erratics from anywhere visited so far in the Amundsen Sea Embayment (Johnson et al., 2020).

- 25 **TUR-117 (451 m a. s. l.):** Granite erratic boulder recovered from relatively flat surface of the lower Turtle Rock platform. The lithology is exotic, and the shape is well-rounded suggesting long-distance subglacial transport, the degree of weathering is minor.

**TUR-123 (639 m a. s. l.):** Granite erratic boulder recovered from the upper slope of Turtle Rock. The lithology is exotic, and the shape is sub-rounded suggesting long-distance subglacial transport, degree of weathering is moderate.

- 30 **TUR-132 (446 m a. s. l.):** Granite erratic boulder recovered from relatively flat surface of the lower Turtle Rock platform. Lithology is exotic and the shape is sub-rounded suggesting long-distance subglacial transport, the degree of weathering is moderate to slight.



35 **Figure S2.** TUR 132 sample location at Turtle Rock and transect line with E-W topographic profile. Satellite imagery from DigitalGlobe products, © WorldView-2 DigitalGlobe, Inc., a Maxar company.

### SCORIA CONE

- 40 CIN samples were recovered from a parasitic scoria cone ~ 1.5 km west of Kay Peak ridge which comprises of two separate outcrops: A (Fig 3.S3) and B (Fig 3.S4). There is evidence to suggest the lower outcrop was covered by ice for a non-zero duration during the late Holocene. The scoria cone outcrops are well described in (Adams et al., 2022).

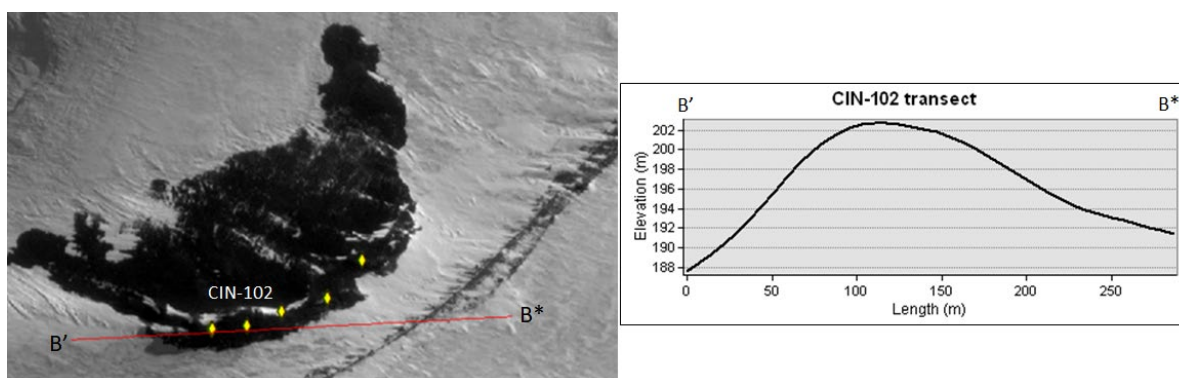


**Figure S3.** CIN-102 sample location at scoria cone outcrop A and transect with E-W topographic profile. Satellite imagery from DigitalGlobe products, © WorldView-2 DigitalGlobe, Inc., a Maxar company.

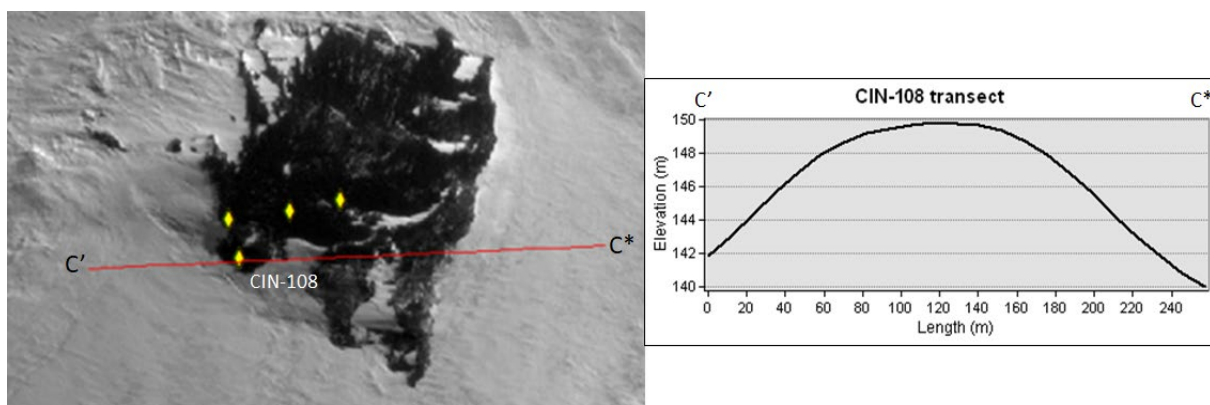


**Figure S4.** CIN-108 sample location at scoria cone outcrop B and transect line with E-W topographic profile. Satellite imagery from DigitalGlobe products, © WorldView-2 DigitalGlobe, Inc., a Maxar company.

**CIN-102 (239 m a. s. l.)** Gneiss erratic of similar lithology to Kay Peak, so there is potential it has been transported from a short distance. The shape of the erratic is subrounded to subangular, and the degree of weathering on the sample is moderate.

**CIN-108 (181 m a.s.l ):** Sub-rounded erratic of exotic granite lithology, suggesting probable long-distance transport, displays a moderate degree of weathering.

**CIN-112 (179 m a. s. l.):** Sub-rounded erratic of aplite lithology, suggesting probable long-distance transport, although a small amount of aplite has also been documented at Kay Peak, sample displays a moderate degree of weathering.

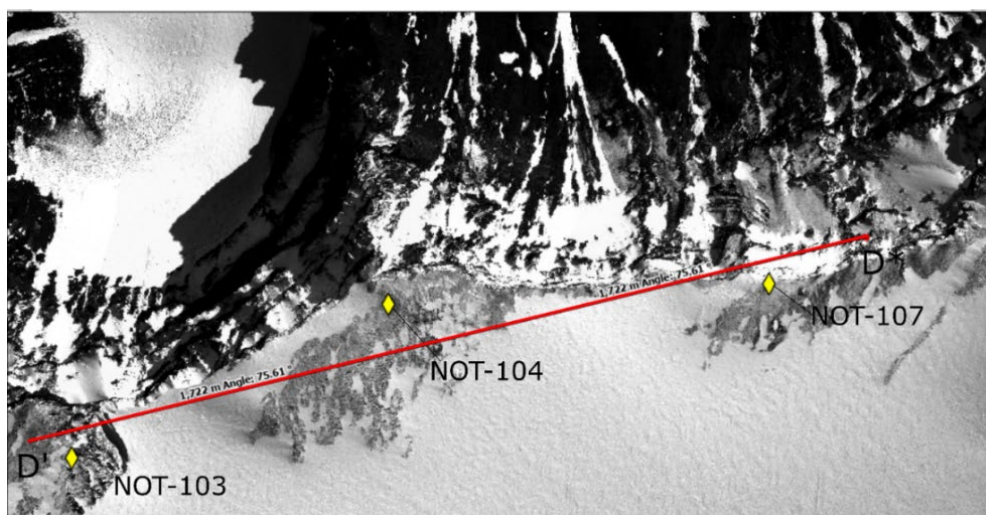
### NOTEBOOK CLIFFS

The NOT samples were recovered from a broad basaltic platform at ~ 900 m a. s. l at the top of Notebook Cliffs (Johnson et al., 2020), the outcrop also contains evidence of hyaloclastite. Cliffs on the northern side are near vertical, but the top is relatively flat and of high elevation. Notably many fewer erratics at Notebook Cliffs than exhibited at lower elevation sites such as nearby Icefall Nunatak (Johnson et al., 2020).

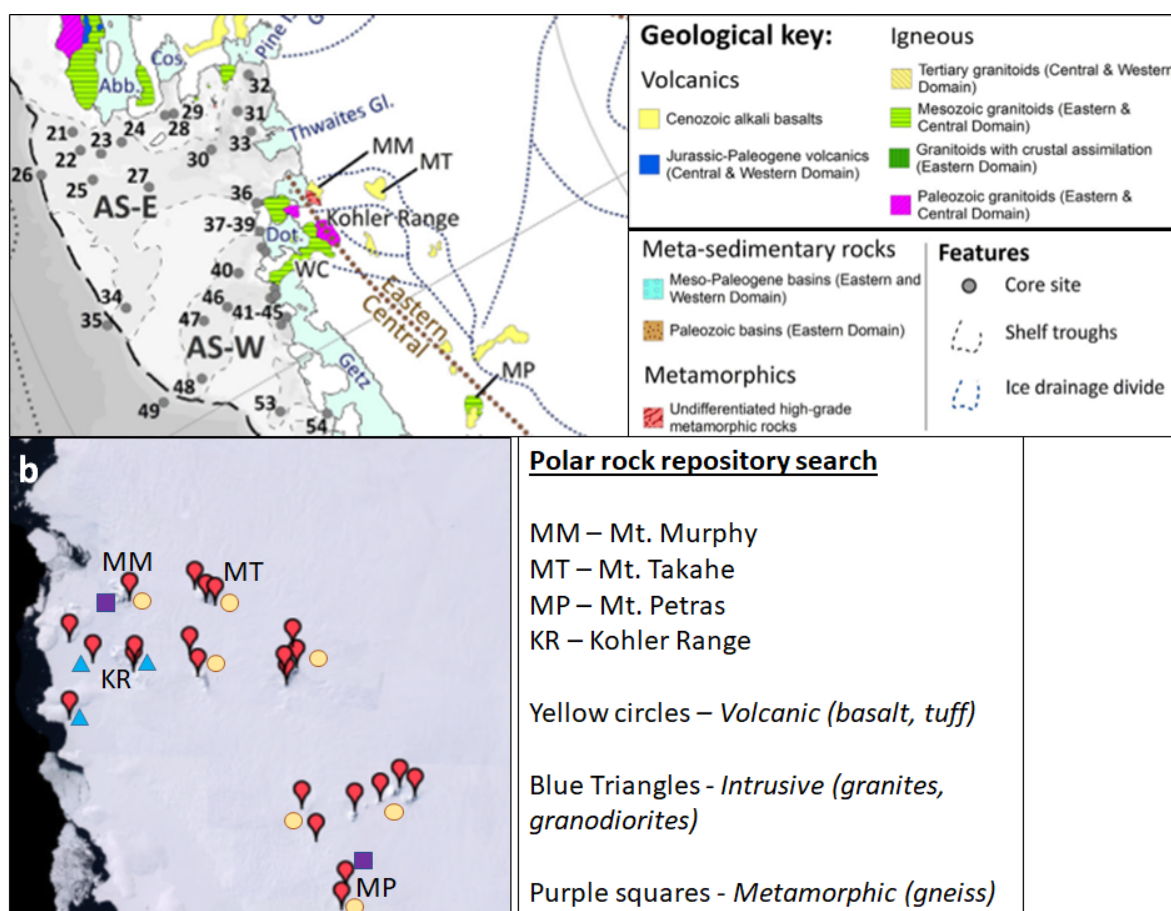
**NOT-103 (852 m a. s. l.):** Subangular erratic of granite lithology, lithology is exotic at Notebook Cliffs which is comprised of mafic rock (basalt and hyaloclastite). Degree of weathering is minor.

**NOT-104 (893 m a. s. l.):** Subangular erratic of granite lithology, Notebook Cliffs is comprised of mafic rock (basalt and hyaloclastite), so lithology is exotic. Sample is moderately weathered with evidence of slight pitting on its surface.

**NOT-107 (885 m a. s. l.):** Subangular erratic of granite lithology, Notebook Cliffs is comprised of mafic rock (basalt and hyaloclastite), so lithology is exotic. Degree of weathering is minor.



70 **Figure S5.** Locations of samples NOT-103, NOT-104 and NOT-107 at Notebook Cliffs. Satellite imagery from DigitalGlobe products, © WorldView-2 DigitalGlobe, Inc., a Maxar company.



75 **Figure S6 (Panel a).** Map from provenance study compiling lithology of major outcrops of exposed rock, blue dotted lines represent present ice divides, dashes black line represents shelf edge, taken from (Simões Pereira et al., 2018) **(Panel b)** Polar rock repository database search of areas of exposed rock upstream of Mt Murphy as well as in the wider area of the Amundsen Sea Embayment and Marie Byrd Land. Map layer taken from and rock sample data points courtesy of the Polar Rock Repository Database <https://prr.osu.edu/> [Accessed 22.04.24]

80 **Figure S7.** Photos of samples analysed for both  $^{10}\text{Be}$  and in situ  $^{14}\text{C}$  in this study. Exposure ages with  $1\sigma$  external uncertainties for  $^{10}\text{Be}$ , in situ  $^{14}\text{C}$  and in situ  $^{14}\text{C}$  replicate measurements are shown below each image.



**NOT-103**

$^{10}\text{Be}$  -  $9.4 \pm 0.6$  ka

$^{14}\text{C}$  -  $3.8 \pm 0.4$  ka



**NOT-104**

$^{10}\text{Be}$  -  $8.6 \pm 0.6$

$^{14}\text{C}$  -  $4.1 \pm 0.4$  ka



**NOT-107**

$^{10}\text{Be}$  -  $8.9 \pm 0.9$

$^{14}\text{C}$  -  $5.2 \pm 0.6$  ka



**TUR-117**

$^{10}\text{Be}$  -  $6.7 \pm 0.5$  ka

$^{14}\text{C}$  -  $3.1 \pm 0.3$  ka

$^{14}\text{C R}$  -  $8.2 \pm 1.1$  ka



**TUR-123**

$^{10}\text{Be}$  -  $10.3 \pm 0.7$  ka

$^{14}\text{C}$  -  $3.8 \pm 0.4$  ka



**TUR-132**

$^{10}\text{Be}$  -  $6.6 \pm 0.5$  ka

$^{14}\text{C}$  -  $7.9 \pm 1.0$  ka

$^{14}\text{C R}$  -  $7.4 \pm 0.9$  ka



**CIN-102**

$^{10}\text{Be}$  -  $7.5 \pm 0.5$  ka

$^{14}\text{C}$  -  $9.0 \pm 1.3$  ka



**CIN-108**

$^{10}\text{Be}$  -  $6.2 \pm 0.4$  ka

$^{14}\text{C}$  -  $6.3 \pm 0.7$  ka

$^{14}\text{C R}$  -  $7.8 \pm 1.0$  ka



**CIN-112**

$^{10}\text{Be}$  -  $6.6 \pm 0.4$  ka

$^{14}\text{C}$  -  $3.4 \pm 0.3$  ka

$^{14}\text{C R}$  -  $7.2 \pm 0.9$  ka

## Supplement S2 – Additional Sensitivity Analyses

### Mt Murphy alternative blank

We present a further sensitivity analysis on the impact of altering the blank correction value on replicate in situ  $^{14}\text{C}$  concentrations (and exposure ages). We use an alternative blank correction of  $3.99 \pm 1.25 \times 10^4$  atoms ( $n = 5$ ) based on the mean and standard deviation of process blanks reported from Tulane laboratory from 03/08/2021 – 12/10/2021 (see Figure S8b). These process blanks represent a change from “thick” 3 mm tubes to a “thin” 1.5 mm mullite tubes for  $^{14}\text{C}$  extraction (Table S5, Balco et al., 2023) and are the blank data closest in time to replicate in situ  $^{14}\text{C}$  concentrations. The alternative blank (BI-2) resulted in poorer reproducibility of initial and replicate situ  $^{14}\text{C}$  ages (3 of 4 did not reproduce at  $1\sigma$  external uncertainty) and discordance between 3 of 4 replicate in situ  $^{14}\text{C}$  ages and corresponding  $^{10}\text{Be}$  ages (Figure S8b). Therefore, this additional sensitivity analysis does not alter our conclusions from results using the blank correction values of 4.53 and 7.14 reported by Tulane.

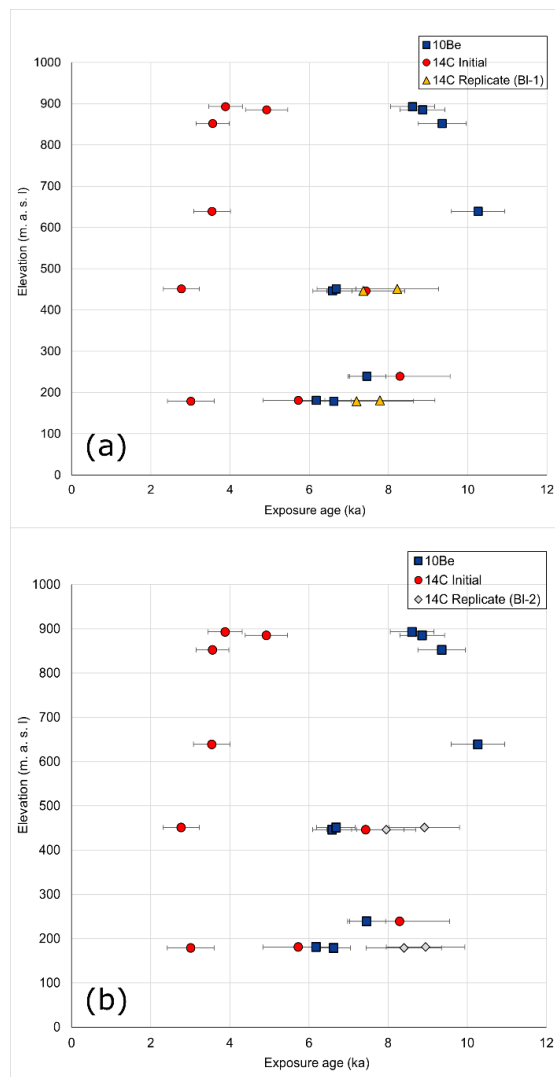
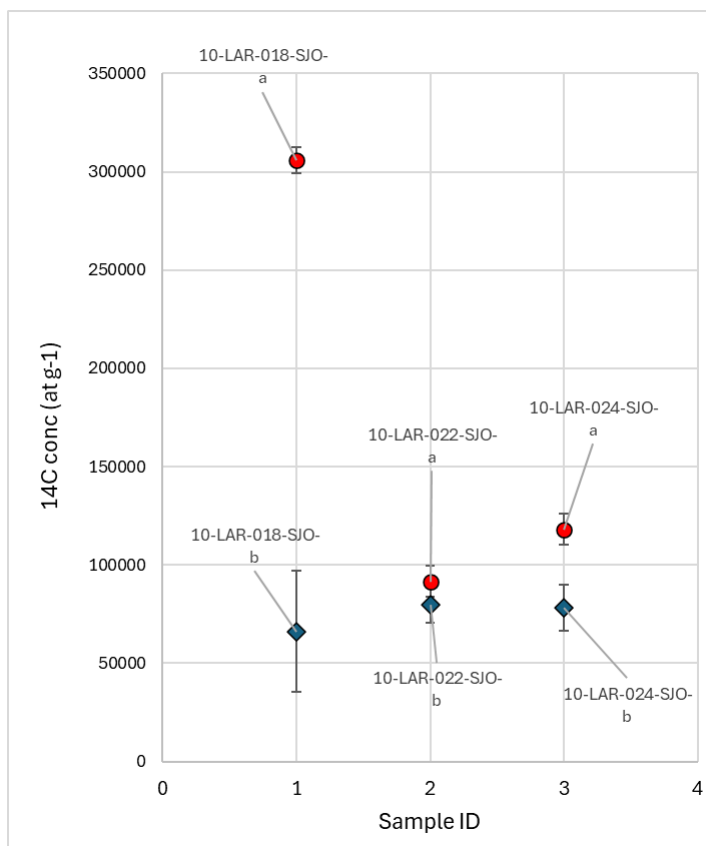


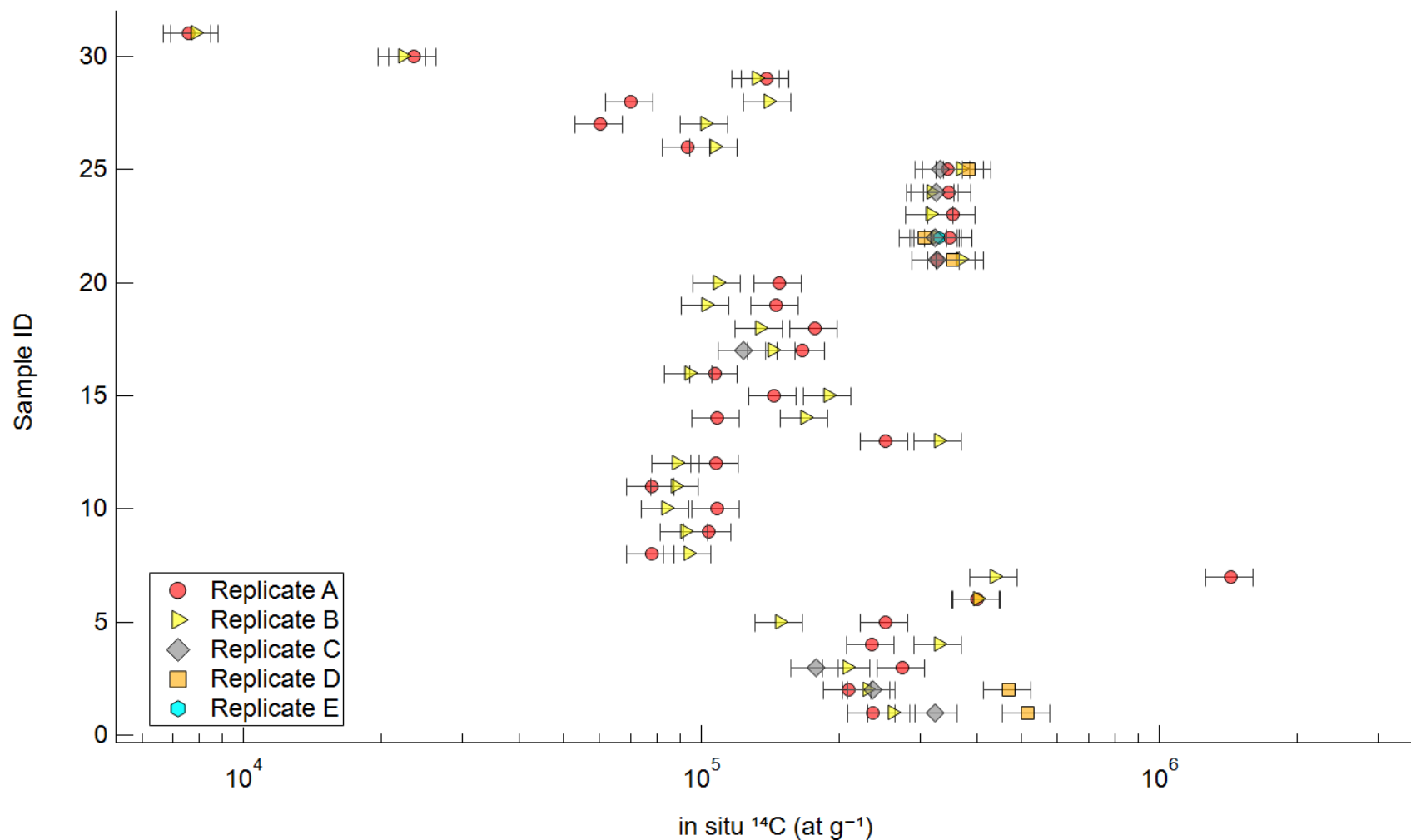
**Figure S8.** Additional sensitivity analysis comparing a) replicate in situ  $^{14}\text{C}$  concentrations corrected using blank value of  $7.14 \pm 3.50 \times 10^4$  atoms presented in Section 4.2, which represent the blank value reported by Tulane, and the standard deviation of all process blanks measured at Tulane from 2019-2021 (BI-1) and b) blank correction of  $3.99 \pm 1.25 \times 10^4$  atoms based on mean and standard deviation of process blanks reported from Tulane laboratory from 03/08/2021 – 12/10/2021. These are the closest process blanks reported in time to in situ  $^{14}\text{C}$  replicate measurements and represent a change from a “thick” 3 mm mullite tube to a “thin” 1.5 mm mullite tube for  $^{14}\text{C}$  extraction (BI-2). Note initial in situ  $^{14}\text{C}$  concentrations are corrected using a blank of  $7.44 \pm 4.16 \times 10^4$  atoms ( $n = 6$ , mean and standard deviation of process blanks bracketing initial measurements) in both plots.

## 105 Sjøgren Glacier Sensitivity Analysis

Here, we perform a sensitivity analyses on initial and replicate in situ  $^{14}\text{C}$  concentrations measured from Sjøgren Glacier. A CRONUS-A concentration of  $5.18 \times 10^5$  atoms  $\text{g}^{-1}$  was measured close to initial in situ  $^{14}\text{C}$  extractions from Sjøgren Glacier (25/09/2018 – 19/10/2018) and a CRONUS-A concentration of  $6.69 \times 10^5$  atoms  $\text{g}^{-1}$  close to the period of replicate in situ  $^{14}\text{C}$  measurements (04/09/2020 – 30/09/2020). We renormalize the Sjøgren Glacier in situ  $^{14}\text{C}$  concentrations (based on the value of  $6.12 \pm 0.32 \times 10^5$  atoms  $\text{g}^{-1}$  reported in Goehring et al., 2019) by the CRONUS-A values closest in time to initial and replicate samples respectively. We also assign the same blanket 10 % uncertainty based on the standard deviation of all CRONUS-A data reported from Tulane as we did for the Mt Murphy in situ  $^{14}\text{C}$  concentrations. Replicate measurements for 10-LAR-018-SJO and 10-LAR-024-SJO still do not reproduce within uncertainty. The same 2 of 3 in situ  $^{14}\text{C}$  concentrations measured in samples 10-LAR-018-SJO and 10-LAR-024- from Sjøgren Glacier which did not overlap within the  $\pm 6\%$  uncertainty (Figure 12) still do not reproduce. Therefore, our conclusions drawn from these in situ  $^{14}\text{C}$  replicate measurements from Sjøgren Glacier are unchanged.



120 **Figure S9.** Sjøgren Glacier in situ  $^{14}\text{C}$  concentrations renormalized to CRONUS-A measurements made closest in time to in situ  $^{14}\text{C}$  extractions of Sjøgren Glacier samples. We apply a 10 % uncertainty to the in situ  $^{14}\text{C}$  concentrations.



125 **Figure S10.** In situ  $^{14}\text{C}$  concentrations in ICE-D for which one or more replicate measurements have been made on the same sample ( $n = 31$ ). Same samples are displayed as in Fig. 10 (main text) showing  $2\sigma$  uncertainty on measurement concentrations based on reproducibility analysis of CRONUS-A at Tulane extraction laboratory. Graph indicates that 15 of 31 samples continue to exhibit one or more in situ  $^{14}\text{C}$  measurement concentrations which do not reproduce at  $2\sigma$ .

### Supplement S3: Comparison of excess scatter of in situ <sup>14</sup>C and <sup>10</sup>Be data from Mt Murphy

Due to the large scatter in ages observed from in situ <sup>14</sup>C measurements along the elevation profile from Mt Murphy (Balco et al., 2023; Johnson et al., 2020), we chose to compare in situ <sup>14</sup>C and <sup>10</sup>Be scatter from the scoria cone and Kay Peak (see Fig. 1a). Using sites that are geographically proximal and at similar elevation minimises additional variation in non-paired exposure age measurements that can arise from inherent uncertainties in production rate scaling when comparing two nuclides. We calculated the error in excess of analytical uncertainty separately for both the <sup>10</sup>Be dataset from scoria cone and in situ <sup>14</sup>C dataset from Kay Peak using the following steps. First we performed a linear regression analyses of the age vs elevation distribution of the exposure ages to obtain the residuals of the least squared fit to the dataset (Bevington and Robinson, 1993). We then performed a bootstrap uncertainty analysis by resampling (sampling with replacement) the residuals determined from the original linear regression model. We fit a new regression model to the resampled data, resampling the original dataset 1000 times. We then calculated the excess scatter in our dataset using the standard deviation of the distribution of regression models determined from resampled residuals.

We omitted three <sup>10</sup>Be exposure ages from erratic cobbles from Kay Peak that are all > ~10 ka from the statistical analysis because the original study identified inheritance in those samples (Johnson et al., 2020). We did not omit any of the in situ <sup>14</sup>C ages from statistical analysis because all in situ <sup>14</sup>C exposure ages postdate the onset of the Holocene (< 11.7 ka), indicating a negligible amount of nuclide inheritance. Data includes in situ <sup>14</sup>C measured in bedrock samples from Kay Peak ridge ( $n = 17$ ) and initial in situ <sup>14</sup>C concentrations measured in erratics ( $n = 3$ ) from scoria cone.

We then calculated the additional error in excess of AMS measurement uncertainty for both the in situ <sup>14</sup>C sample set and the <sup>10</sup>Be sample set using the following equation:

$$\text{Excess Uncertainty} = (S^2) - (\bar{x}\sigma^2) \quad \text{Eq. S3.1}$$

where  $S$  denotes the standard deviation of the in situ <sup>14</sup>C or <sup>10</sup>Be residuals, i.e., total scatter in each respective dataset (in years) and  $\bar{x}\sigma$  refers to the average analytical uncertainty of the collective in situ <sup>14</sup>C or <sup>10</sup>Be exposure ages in each respective sample set (also in years).

#### In situ <sup>14</sup>C and <sup>10</sup>Be bootstrapping results from Mt Murphy

We now compare results from our statistical analysis of scoria cone and Kay Peak exposure age datasets. The in situ <sup>14</sup>C derived line of best fit indicates deglaciation began at 7.1 ka (uncovering of surfaces at 350 m a. s. l.) and surfaces at 125 m a. s. l. were uncovered by 6.1 ka. The <sup>10</sup>Be-derived line of best fit indicates that deglaciation (uncovering surfaces at 350 m a. s. l.) began slightly earlier, at 8.3 ka, with surfaces at 125 m a. s. l. uncovered slightly later, at 5.7 ka. The age range for deglaciation is similar for the two datasets and the data broadly follow the same linear trend (Fig. 6). This similarity strongly suggests that an accurate chronology is being achieved with both nuclides at this site, and there is minimal inheritance in the samples. At 95 % confidence, the degree of scatter of the in situ <sup>14</sup>C dataset (Fig. S11a) is greater than the <sup>10</sup>Be dataset (Fig. S11b).

The in situ <sup>14</sup>C sample set ( $n = 20$ ) has a residual standard deviation of 1957 years and the <sup>10</sup>Be sample set has a residual standard deviation of 225 years ( $n = 12$ ) (Table 2). The average internal uncertainty of the in situ <sup>14</sup>C exposure ages is 641 years, whilst the average internal uncertainty of the <sup>10</sup>Be exposure ages is 222 years. The unquantified uncertainty remaining from scatter in the in situ <sup>14</sup>C exposure age dataset is 1849 years, this is considerably larger than the excess uncertainty for the <sup>10</sup>Be exposure ages (37 years) and suggests additional uncertainty beyond stated analytical uncertainties is contributing towards increased scatter visible in the in situ <sup>14</sup>C dataset.

**Table S6** Summary statistics of bootstrapping results of in situ  $^{14}\text{C}$  derived exposure ages ( $n=20$ ) compared to summary statistics of  $^{10}\text{Be}$  Kay derived exposure ages ( $n=12$ ) from Kay Peak and scoria cone sites. The purpose of the statistical analysis is to identify unquantified sources of uncertainty.  $^{10}\text{Be}$  inheritance is a known contributor to scatter in  $^{10}\text{Be}$  measurements so any samples strongly suspected of contributing scatter to the  $^{10}\text{Be}$  dataset due to inheritance have been removed.

Reported Metric	$^{14}\text{C}$ Kay Peak & scoria cone	$^{10}\text{Be}$ Kay Peak & scoria cone
Std Dev. Residuals (yrs)	1957	225
Av. analytical error $1\sigma$ (yrs)	641	222
Av. external error $1\sigma$ (yrs)	834	453
Error in excess of analytical uncertainty (yrs)	1849	37

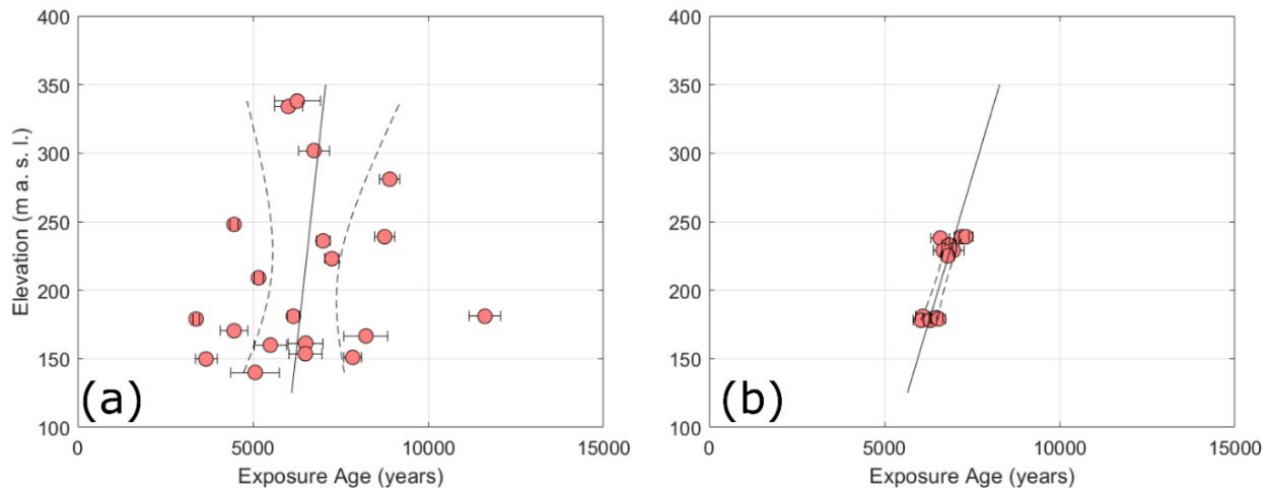


**Figure S11:** Results of bootstrapped linear regression for Kay Peak/ scoria cone (a) in situ  $^{14}\text{C}$  dataset ( $n=20$ ) and (b)  $^{10}\text{Be}$  dataset ( $n=12$ ). In both panels exposure ages are shown with  $1\sigma$  internal uncertainties. The solid line in each plot represents the line of best fit determined from linear regression, and the dashed lines represent the 95 % confidence interval. Note  $^{10}\text{Be}$  apparent exposure ages strongly suggesting nuclide inheritance (Johnson et al., 2020) were not included in the bootstrapping analysis. Exposure ages presented in both plots have been calculated using the LSDn scaling scheme.

#### 4.1.1 A statistical comparison of in situ $^{14}\text{C}$ and $^{10}\text{Be}$ datasets at scoria cone and Kay Peak

The statistical analysis (Table S6) indicates almost all scatter in the distribution of  $^{10}\text{Be}$  exposure ages which are of Holocene age and not removed as outliers from scoria cone and Kay Peak sites, can be accounted for by the reported analytical uncertainty in  $^{10}\text{Be}$  AMS measurements. This finding is consistent with improvements in AMS precision and reproducibility reported from CRONUS-A and CRONUS-N intercomparison materials (Corbett et al., 2022; Jull et al., 2015). However, uncertainty in excess of measurement uncertainty of the in situ  $^{14}\text{C}$  exposure ages (1849 years), exceeds the average in situ  $^{14}\text{C}$  measurement uncertainty (641 years) reported for Kay Peak and scoria cone elevation-age datasets (Fig. S11).

Exposure ages for both in situ  $^{14}\text{C}$  and  $^{10}\text{Be}$  used in our bootstrapping comparison are from the same sample sites: Kay Peak and scoria cone. Very few are however paired  $^{14}\text{C}$ - $^{10}\text{Be}$  measurements from the same sample ( $n=3$ ). Differences in geological scatter of individual samples from both datasets could explain some of the mismatch in excess scatter determined for in situ  $^{14}\text{C}$  and  $^{10}\text{Be}$  exposure ages.

The inclusion of  $^{10}\text{Be}$  exposure ages from Kay Peak that pre-date the Holocene would increase scatter in the  $^{10}\text{Be}$  profile but represent a recognised source of  $^{10}\text{Be}$  scatter from inheritance.  $^{10}\text{Be}$  outliers are generally easier to identify and filter because inheritance can quite obviously increase the apparent exposure age relative to the main population. Scatter observed from the in situ  $^{14}\text{C}$  ages is however large relative to the total amount of inheritance or post-depositional disturbance typically detected in an in situ  $^{14}\text{C}$  measurement due to the short-half-life mitigating for inheritance over multiple glaciations. The removal of  $^{10}\text{Be}$  outliers with inheritance decreases the elevation range of samples used for the  $^{10}\text{Be}$  dataset (180–240 m a. s. l.) relative to the in situ  $^{14}\text{C}$  dataset (150–350 m a. s. l.). Nevertheless, the difference of  $\sim 1800$  years of excess scatter beyond analytical uncertainty for the in situ  $^{14}\text{C}$  exposure age dataset relative to  $^{10}\text{Be}$  exposure age dataset is still significant.

To summarise, the in situ  $^{14}\text{C}$  and  $^{10}\text{Be}$  chronologies are broadly similar with respect to the timing of deglaciation, implying they are equally accurate. There is, however, a significant amount of scatter in the distribution of in situ  $^{14}\text{C}$  exposure ages that cannot be accounted for by the nominal 6 %  $1\sigma$  internal measurement uncertainty for in situ  $^{14}\text{C}$  adopted in many studies (Balco et al., 2019; Nichols et al., 2019). In contrast, uncertainty in  $^{10}\text{Be}$  analytical measurements can account for the scatter observed in the distribution of Holocene  $^{10}\text{Be}$  ages at the site. The two possibilities are 1) unquantified geological scatter is disproportionately impacting in situ  $^{14}\text{C}$  exposure ages in the scoria cone and Kay Peak datasets and 2) in situ  $^{14}\text{C}$  measurement uncertainty is not fully accounting for uncertainties incorporated during sample preparation.

#### **Supplement S4: Assessment of Mt Murphy quartz separates impact on in situ $^{14}\text{C}$ reproducibility**

Mineral elemental impurities which are not fully homogenised within a sample can lead to differences in measured nuclide concentrations, impacting reproducibility (Corbett et al., 2022). In situ  $^{14}\text{C}$  production in silicates (such as

quartz, typically sampled for  $^{10}\text{Be}$ ,  $^{26}\text{Al}$  and  $^{14}\text{C}$  measurements) at SLHL is dominated by oxygen spallation accounting for  $> 90\%$  at SLHL, but also occurs from spallation of Si, Mg, Al and Na (Koester and Lifton, 2023). Modelled in situ  $^{14}\text{C}$  spallogenic production rates for Mg-rich silicates such as olivine, are 7–10 % lower than pure quartz, while Al-rich minerals such as K and Ca feldspars have production rates 12–13 % below quartz. Modelled in situ  $^{14}\text{C}$  production rates for Fe bearing minerals such as fayalite ( $\text{Fe}_2\text{SiO}_4$ ) are as much as 41 % lower than pure quartz (Koester and Lifton, 2023). Trace elements or minerals within the quartz mineral separate can therefore cause differences in the in situ  $^{14}\text{C}$  production rate, impacting reproducibility. We therefore conduct a preliminary examination to determine if trace elemental impurities of Al, Fe, Mg, Ca, Na, Ti, and K measured in Mt Murphy samples following quartz purification (Table S7) impact the spallogenic in situ  $^{14}\text{C}$  production rate and partly account for in situ  $^{14}\text{C}$  repeat analyses which do not reproduce within 6 %  $1\sigma$  (or  $2\sigma$ ) uncertainties.

**Table S7:** Concentration data measured by ICP-OES of major elemental impurities (displayed as weight %) following quartz purification of samples measured for in situ  $^{14}\text{C}$  ( $n = 9$ ). The total sum weight % of elements is displayed, and percentage of each sample which is pure quartz (far right column). This differs from the (Corbett et al., 2022) study which reported elemental analysis results following the majority of Be extraction steps including column chemistry but is appropriate for investigating in situ  $^{14}\text{C}$  reproducibility because situ  $^{14}\text{C}$  analyses are made directly on in situ  $^{14}\text{C}$  gas extracted from the quartz mineral separate.

Sample ID	Al wt %	Fe wt %	Mg wt %	Ca wt %	Na wt %	Ti wt %	K wt %	Total wt %	SiO <sub>2</sub> wt %
CIN-102	0.0147	0.0056	0.0016	0.0020	0.0009	0.0033	0.0063	<b>0.0344</b>	99.9656
CIN-108	0.0031	0.0003	0.0001	0.0007	0.0003	0.0017	0.0001	<b>0.0063</b>	99.9937
CIN-112	0.0035	0.0003	0.0002	0.0008	0.0006	0.0016	0.0004	<b>0.0074</b>	99.9926
NOT-103	0.0079	0.0006	0.0001	0.0006	0.0002	0.0018	0.0001	<b>0.0113</b>	99.9887
NOT-104	0.0052	0.0006	0.0001	0.0004	0.0003	0.0023	0.0009	<b>0.0098</b>	99.9902
NOT-107	0.0043	0.0005	0.0001	0.0006	0.0006	0.0016	0.0007	<b>0.0084</b>	99.9916
TUR-117	0.0026	0.0001	0.0000	0.0007	0.0009	0.0012	0.0008	<b>0.0063</b>	99.9937
TUR-123	0.0089	0.0001	0.0001	0.0008	0.0004	0.0015	0.0000	<b>0.0118</b>	99.9882
TUR-132	0.0017	0.0014	0.0000	0.0012	0.0003	0.0019	0.0000	<b>0.0065</b>	99.9935

Trace element concentrations in Mt Murphy quartz mineral separates were obtained by Inductively Coupled Plasma Optical Emission Spectrometer (ICP-OES) following quartz purification at Imperial College London. We calculated the equivalent weight % of the oxides  $\text{Al}_2\text{O}_3$ ,  $\text{Fe}_2\text{O}_3$ ,  $\text{MgO}$ ,  $\text{CaO}$ ,  $\text{Na}_2\text{O}$ ,  $\text{TiO}_2$ , and  $\text{K}_2\text{O}$  in Mt Murphy samples from the ICP-OES elemental concentration data. We used the MATLAB code of Koester and Lifton (2023) to calculate compositionally dependent, site-specific production rates ( $\text{at g}^{-1} \text{yr}^{-1}$ ) for each Mt Murphy sample measured for in situ  $^{14}\text{C}$  (Table S7). Our analysis shows that 1) the elemental abundance of the target element impurities in the Mt Murphy mineral separates is extremely low for all samples, i.e., the quartz purity of Mt Murphy samples is high ( $> 99.9\%$ ) (Table S7) and 2) trace elemental impurities that persisted in mineral separates following quartz purification do not significantly impact modelled in situ  $^{14}\text{C}$  spallogenic production rates.

**Table S8:** Comparison of modelled in situ  $^{14}\text{C}$  compositionally dependent, site-specific production rates ( $P_{\text{CD}}$ ) for Mt Murphy quartz mineral separates. The in situ  $^{14}\text{C}$  production rate calculated with the elemental impurities measured in the quartz minerals by ICP-OES (Table S4) is contrasted to the in situ  $^{14}\text{C}$  production rate for the same samples assuming they are compositionally 100 %  $\text{SiO}_2$ . Modelled in situ  $^{14}\text{C}$  production rates calculated using the LSDn scaling scheme of (Lifton et al., 2014) and code of Koester and Lifton (2023).

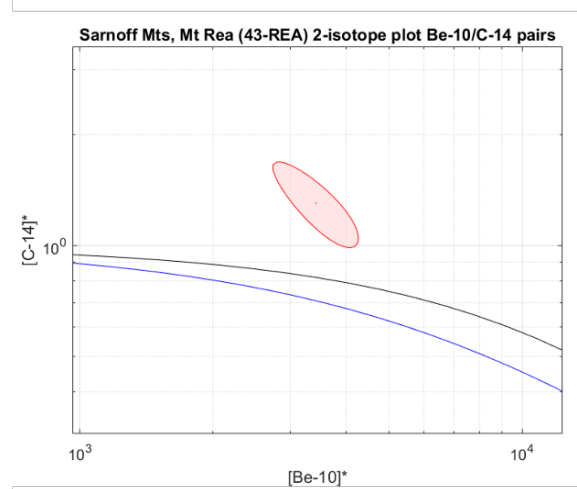
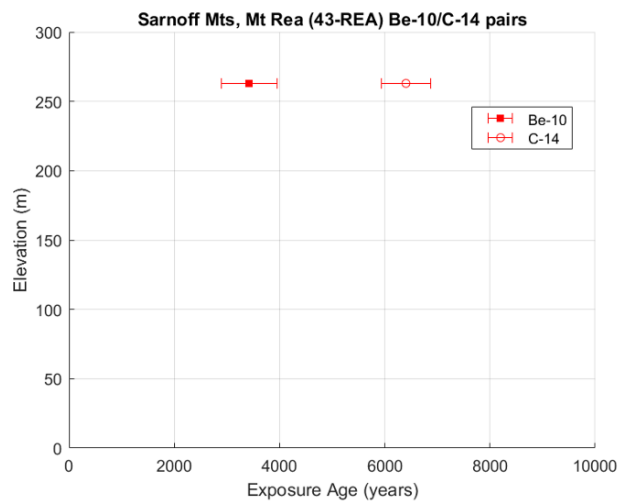
Sample Name	$^{14}\text{C} - ^{10}\text{Be}$	$^{14}\text{C}$ (2 $\sigma$ )	Rep.	Latitude (DD)	Longitude (DD)	Elevation (m a. s. l)	$^{14}\text{C}$ PCD Diff. (%)
CIN-102	concordant	-		-75.21943	-111.02316	239	100.014
CIN-108	concordant	Yes		-75.21652	-111.01973	181	100.002
CIN-112	discordant	No		-75.21628	-111.01796	179	100.002
NOT-103	discordant	-		-75.39144	-111.13985	852	100.003
NOT-104	discordant	-		-75.38863	-111.11753	893	100.003
NOT-107	discordant	-		-75.38818	-111.09055	885	100.003
TUR-117	discordant	No		-75.38110	-111.30660	451	100.002
TUR-123	discordant	-		-75.37061	-111.29230	639	100.003
TUR-132	concordant	Yes		-75.38303	-111.30911	446	100.003

The maximum difference in the in situ  $^{14}\text{C}$  production rate calculated assuming pure  $\text{SiO}_2$  and the elemental composition of Mt Murphy samples measured by ICP-OES (Table S4) is 0.014% for sample CIN-102 (this sample also contains the highest total % weight elemental impurities at 0.03 % or 300 ppm). For all other samples the difference in modelled production rates is < 0.001 % (Table S8). Marginal differences in modelled in situ  $^{14}\text{C}$  production rates of 0.002–0.014 % therefore do not account for in situ  $^{14}\text{C}$  concentrations of Mt Murphy replicate measurements, which are not reproducible using 6 %  $1\sigma$  uncertainties. This preliminary analysis is limited by the small number of replicate samples ( $n = 4$ ). In addition, only production pathways by in situ  $^{14}\text{C}$  by spallation are modelled, while muogenic in situ  $^{14}\text{C}$  production at SLHL constitutes ~20% of total production. Nevertheless, our analysis indicates very low elemental impurities detected in Mt Murphy mineral separates results in extremely small changes to the in situ  $^{14}\text{C}$  production rate and so does not account for observed scatter of up to 100 % between replicate in situ  $^{14}\text{C}$  concentrations from the Mt Murphy dataset. Our evaluation of Mt Murphy samples therefore finds no significant link between low abundances of elemental impurities in quartz mineral separates and in situ  $^{14}\text{C}$  reproducibility. Nevertheless, a more in-depth study similar to Corbett et al., (2022) which assessed impact of quartz impurity in CRONUS-N on  $^{10}\text{Be}$  reproducibility would help improve quantification of in situ  $^{14}\text{C}$  reproducibility. We would, however, suggest a different intercomparison material, e.g., CRONUS-R which is a low-level sample (Fülöp et al., 2019) as being appropriate for this purpose.

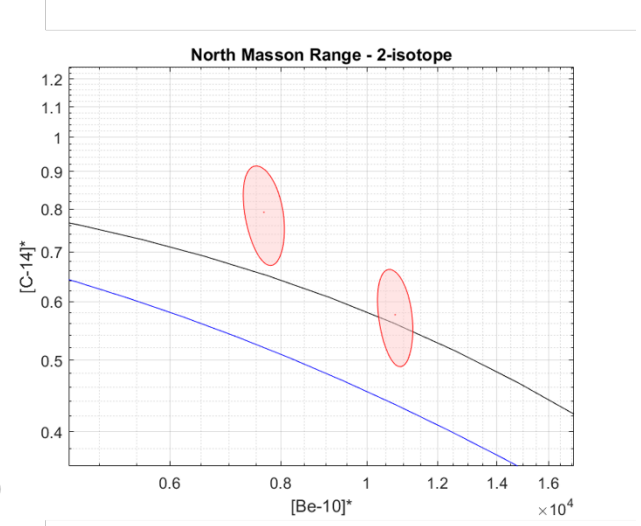
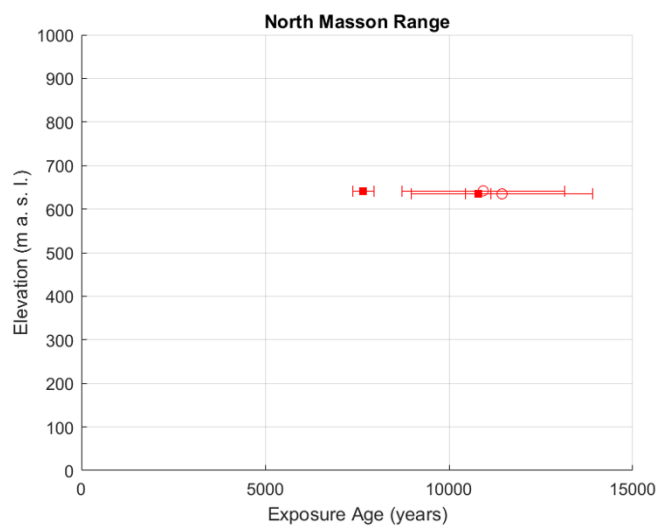
## Supplement S5: Holocene filter age vs elevation plots and paired nuclide diagrams.

This supplement contains exposure age vs elevation plots ( $1\sigma$  uncertainties) and paired nuclide diagrams (68 % error ellipses) displaying all sites were paired in situ  $^{14}\text{C}$ - $^{10}\text{Be}$  exposure ages were extracted from ICE-D [last accessed - 29.03.24] using the Holocene search filter (see Section 2.3). Sites are numbered according to their unique site ID in ICE-D and correspond to numbering in Figure 1, and Table 3 in the main paper. Mt Murphy age vs elevation plots and paired nuclide diagrams (sites 2, 7 and 8) are in the main paper (Fig. 4, Fig. 5).

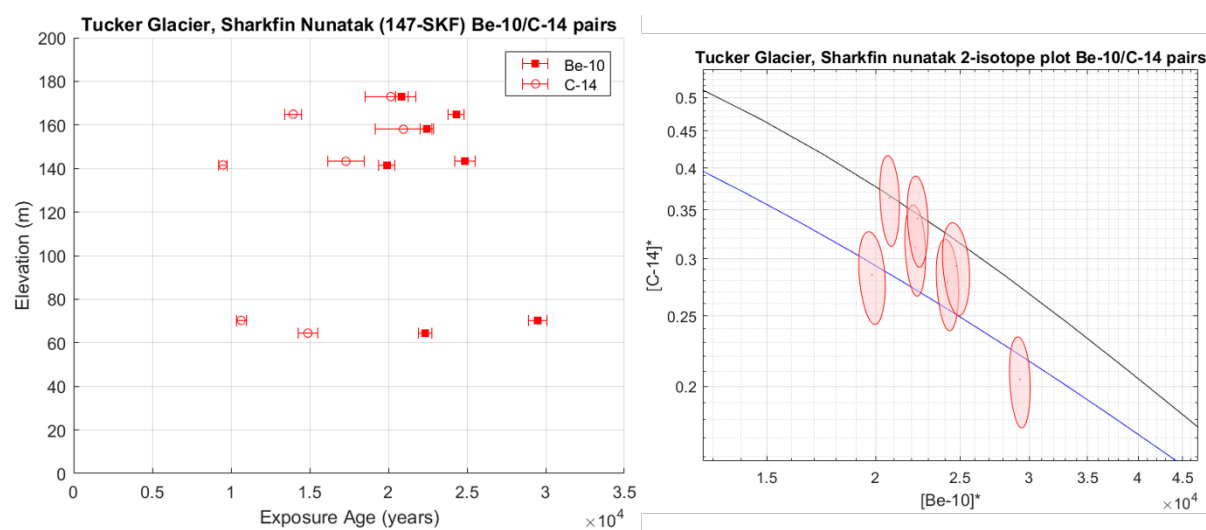
### Site 1: Mt Rea, Sarnoff Mts. (Ross Sea) - Type 3



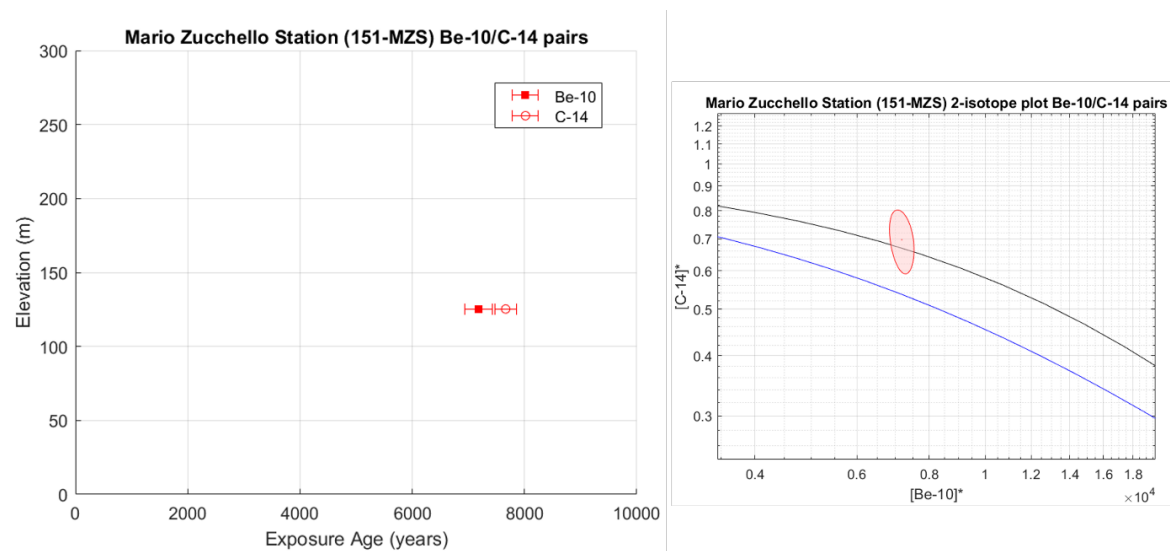
### Site 3: North Masson Range, Framnes Mts (East Antarctica) - Type 1, 3



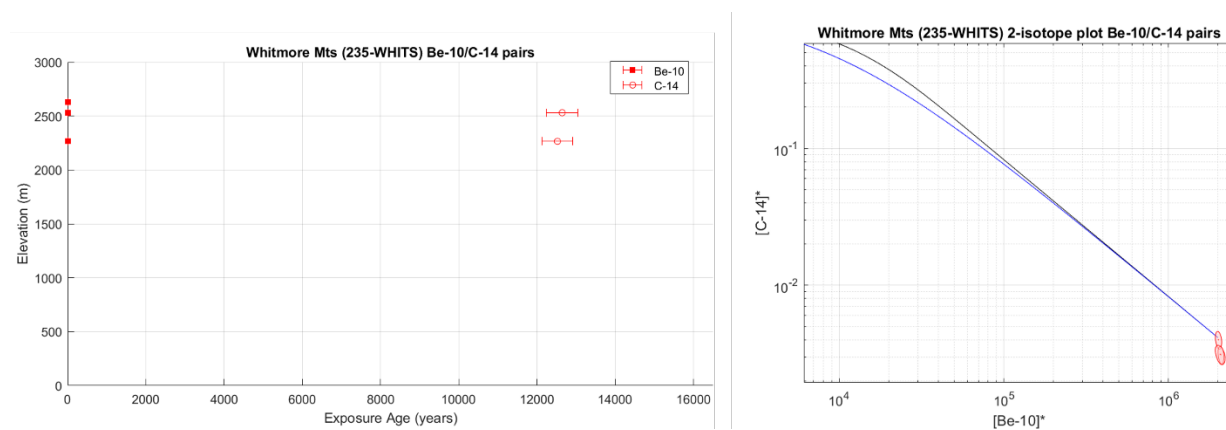
#### Site 4: Sharkfin nunatak, Tucker Glacier (Ross Sea) - Type 1 (2)



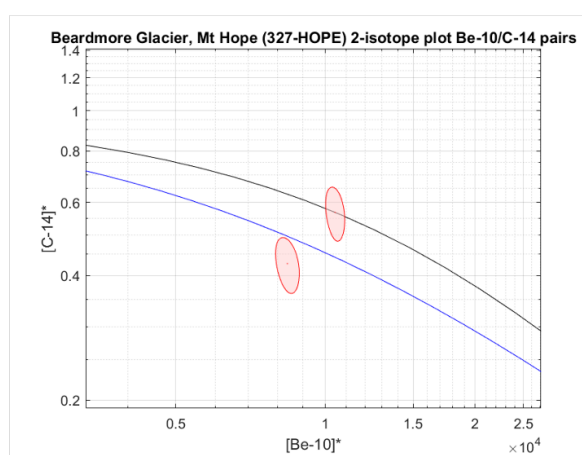
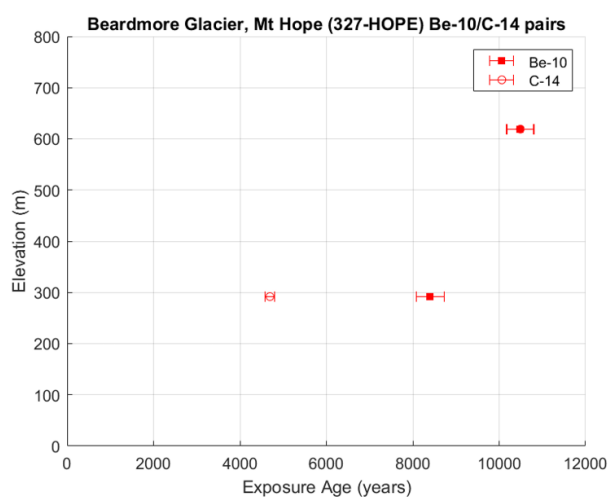
#### 310 Site 5: Mario Zucchelli Station, Terra Nova Bay (Ross Sea) – Type 1



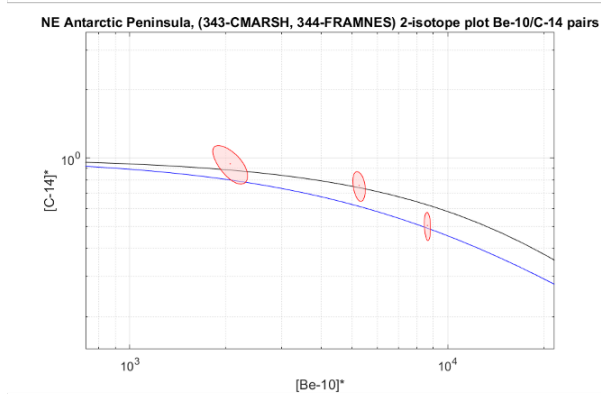
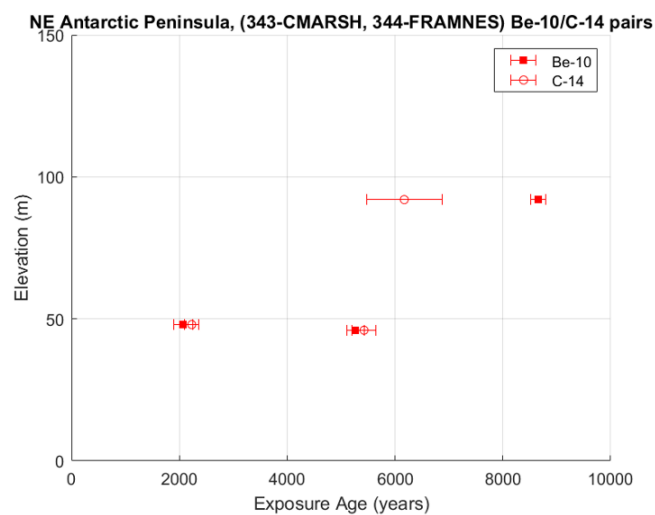
#### Site 6: Mt Whitmore, Whitmore Mts. (Ross Sea) – Type N/A



## Site 9: Mt Hope, Beardmore Glacier (Ross Sea) – Type 1 2

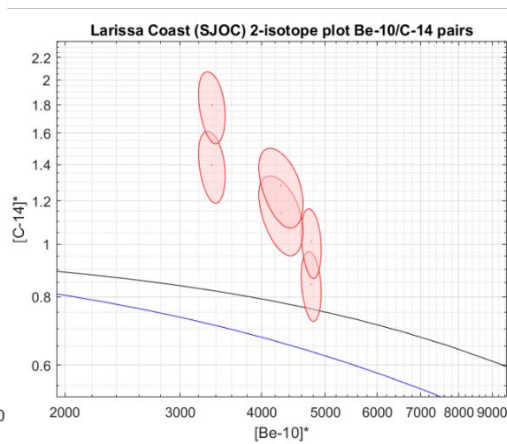
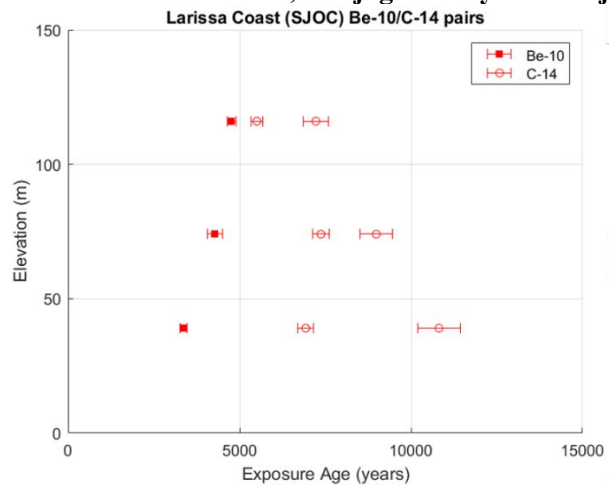


## Site 10 and Site 11: Cape Marsh and Cape Framnes (Antarctic Peninsula) – Type 1 (2)

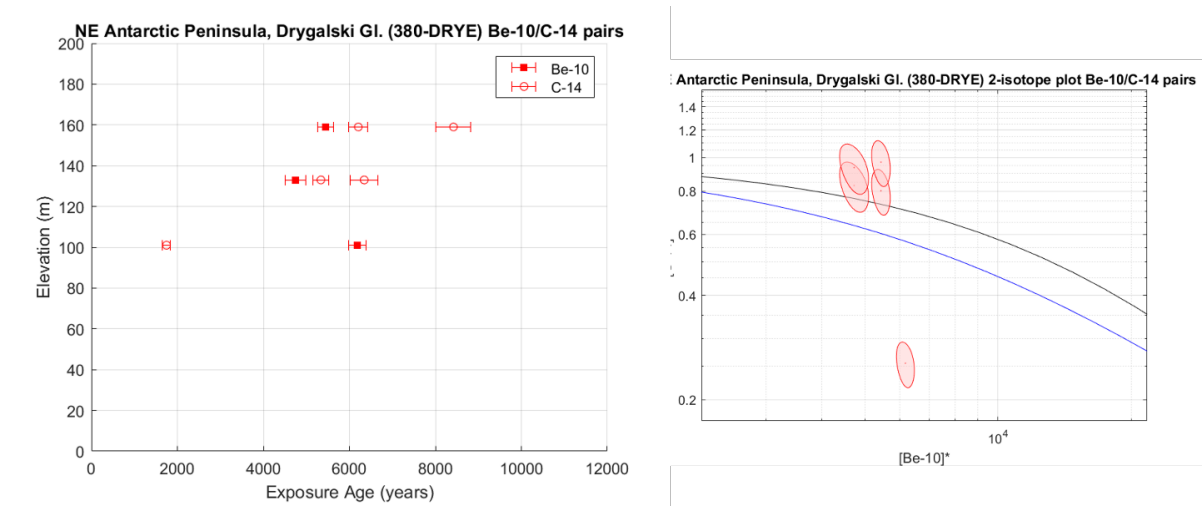


320

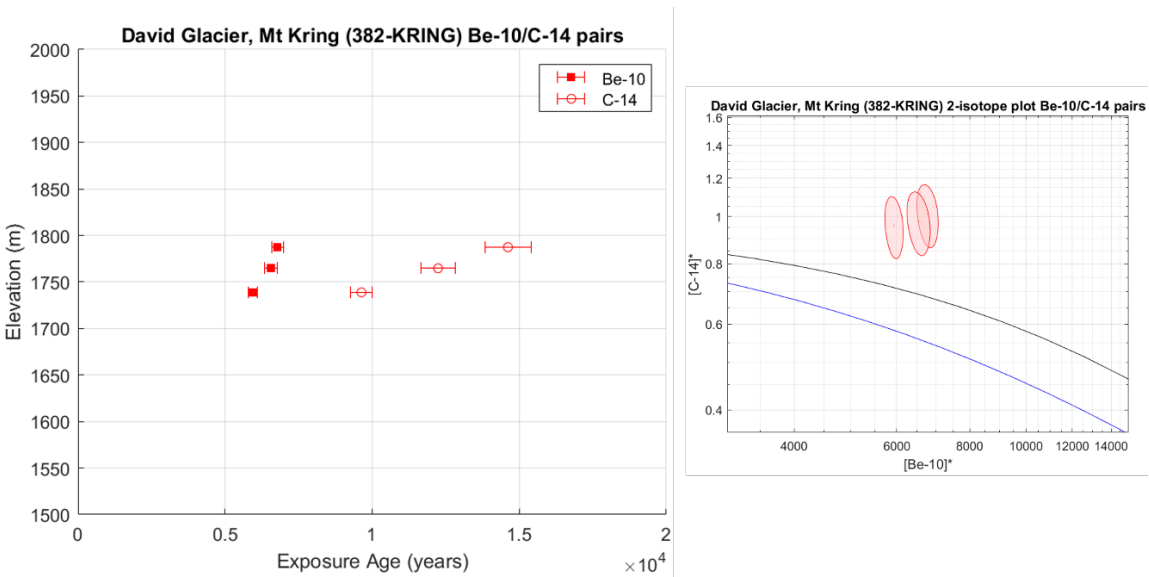
## Site 12: Site C, Sjogren-Boydell Fjord (Antarctic Peninsula) – Type 3



325      **Site 13: Site E, Drygalski Glacier (Antarctic Peninsula) – Type 1 2 3**

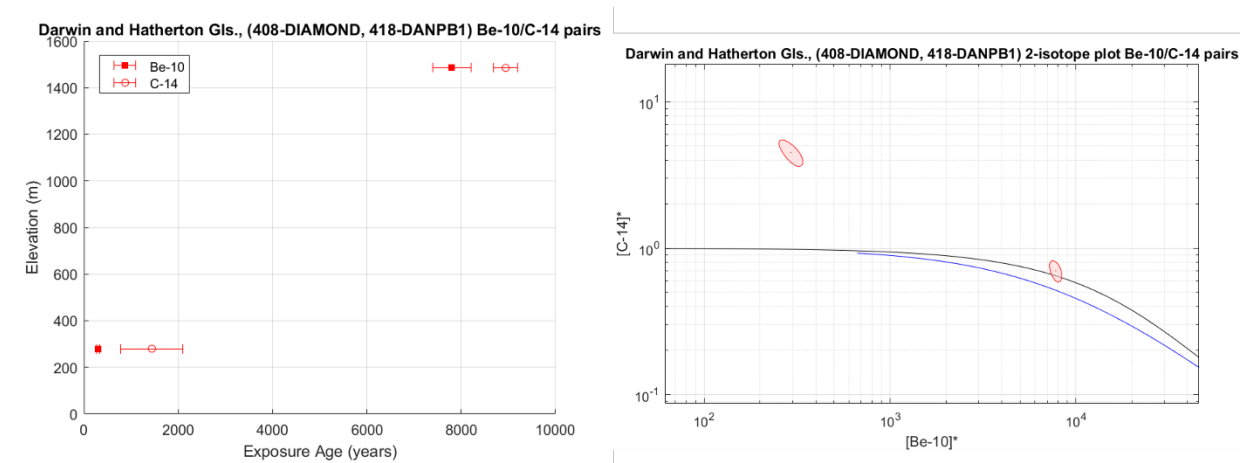


**Site 14: Mt Kring, David Glacier (Ross Sea) – Type 3**

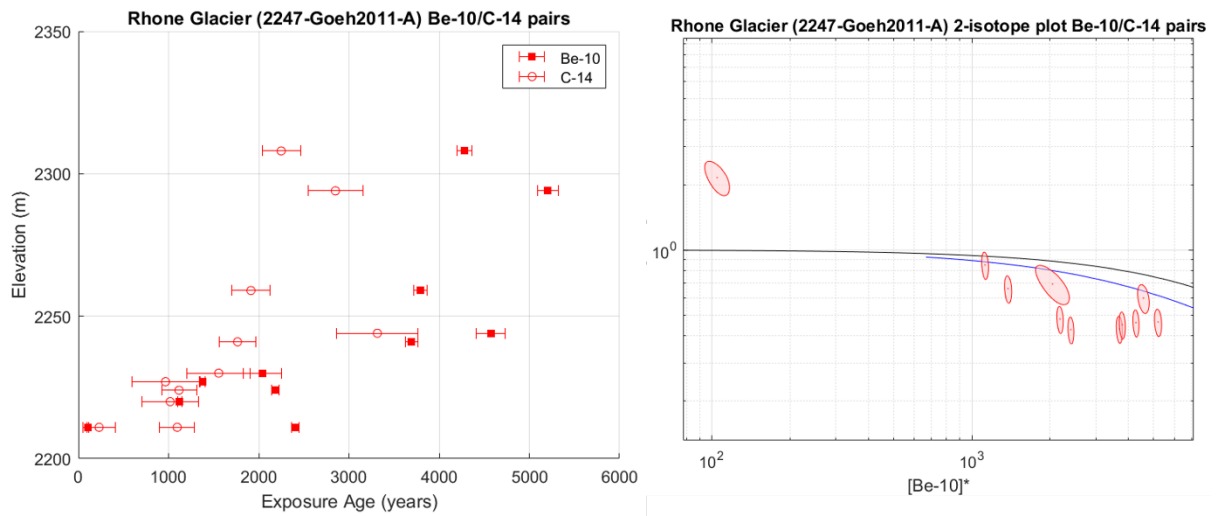


330

**Site 15 and Site 16: Diamond Hill and Danum Plat., Darwin and Hath. Gl. (Ross Sea) - Type 1, 3**

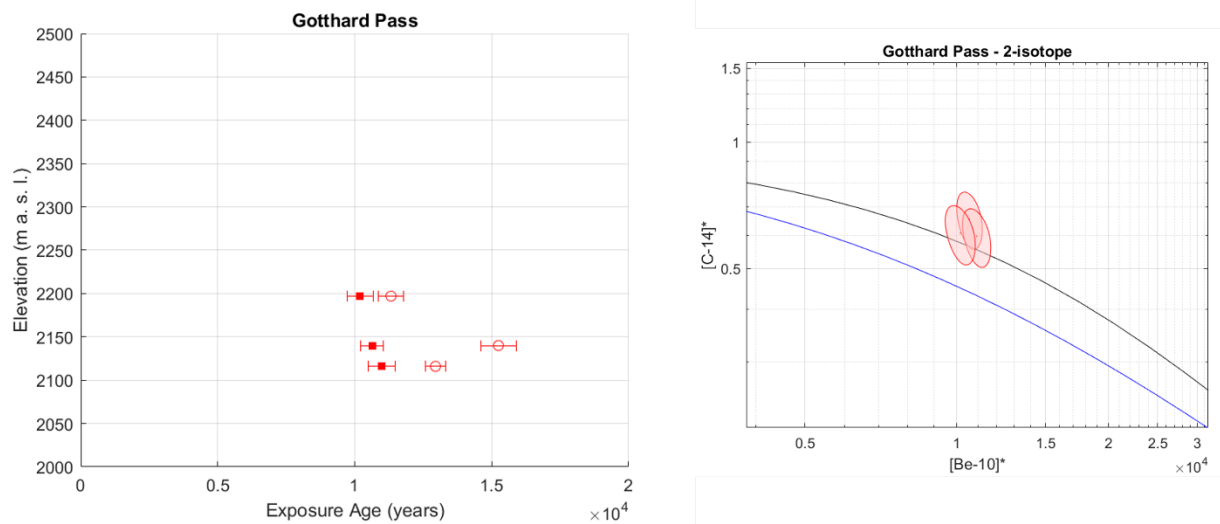


## Site 17: Rhone Glacier, Switzerland (Europe) – Type 2

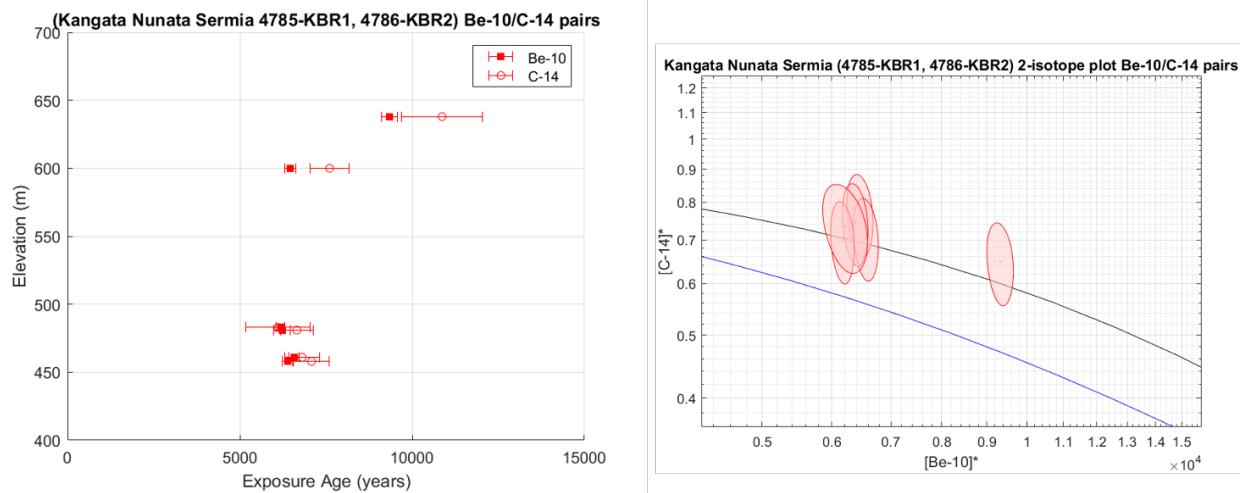


335

## Site 18: Gotthard Pass, Switzerland (Europe) – Type 1

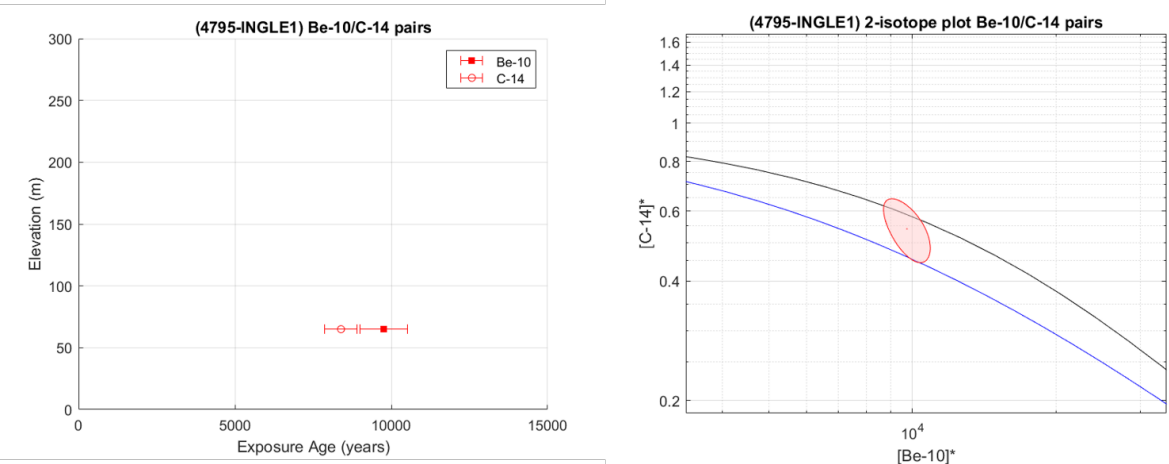


## Site 19 and Site 20: Kangata Nunata Sermia, Greenland – Type 1

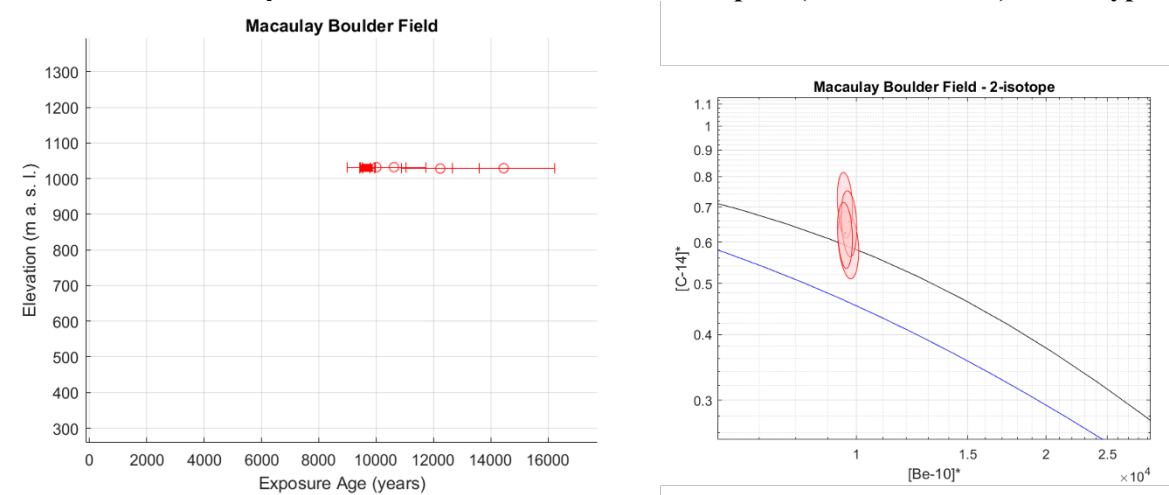


340

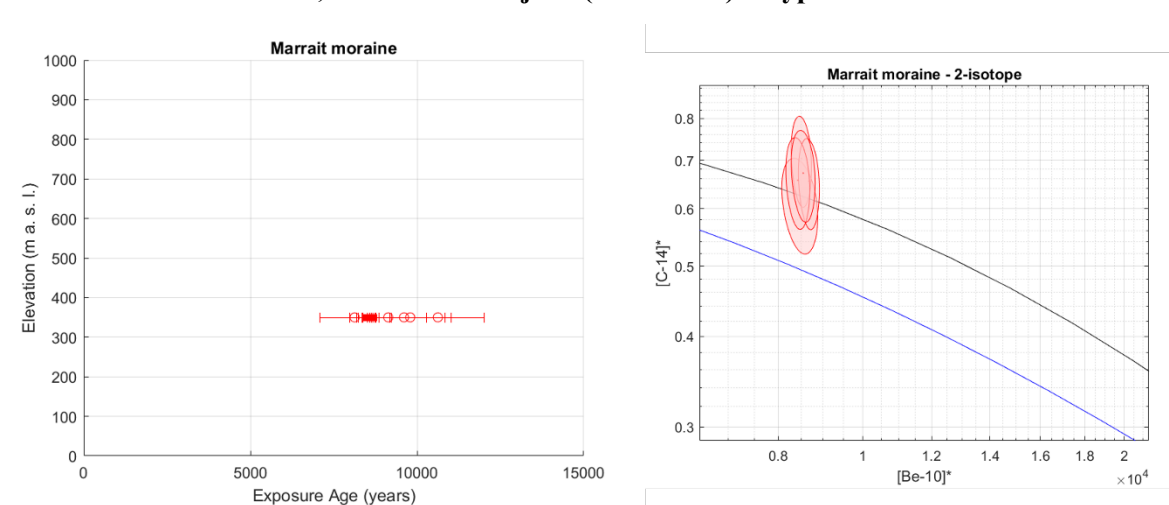
Site 21: Outboard of present margin, Inglefield Land (Greenland) – Type 1



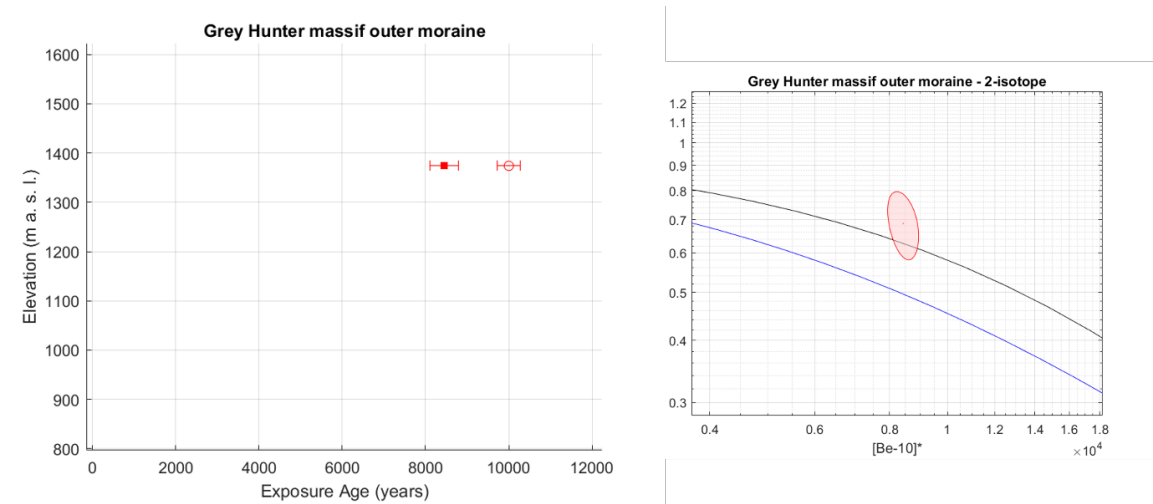
Site 22: Macaulay Boulder Field, Southern Alps (New Zealand) – Type 1



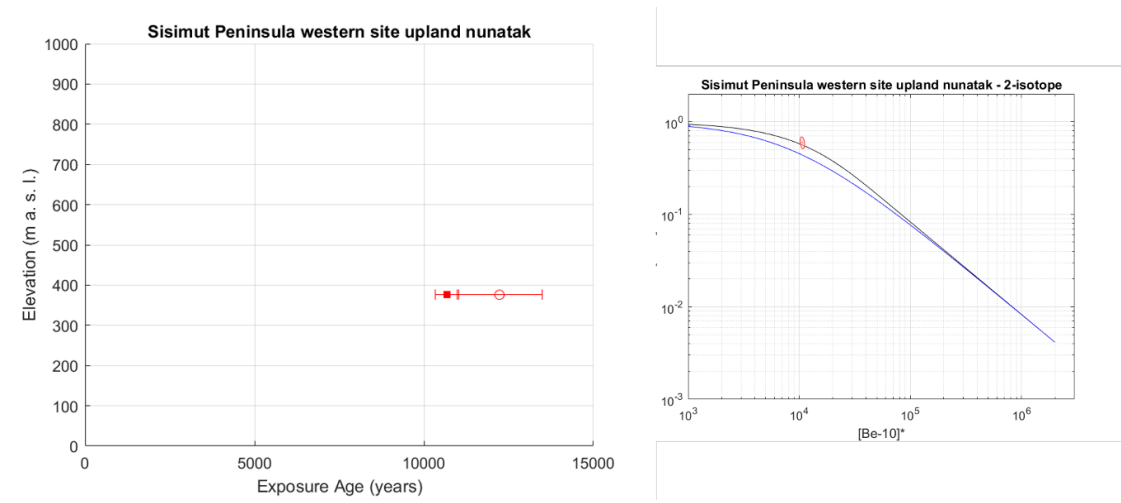
Site 23: Marrait Moraine, Jakobshavn Isfjord (Greenland) – Type 1



Site 24: Grey Hunter Massif, MacArthur Mts. (Yukon) – Type 1

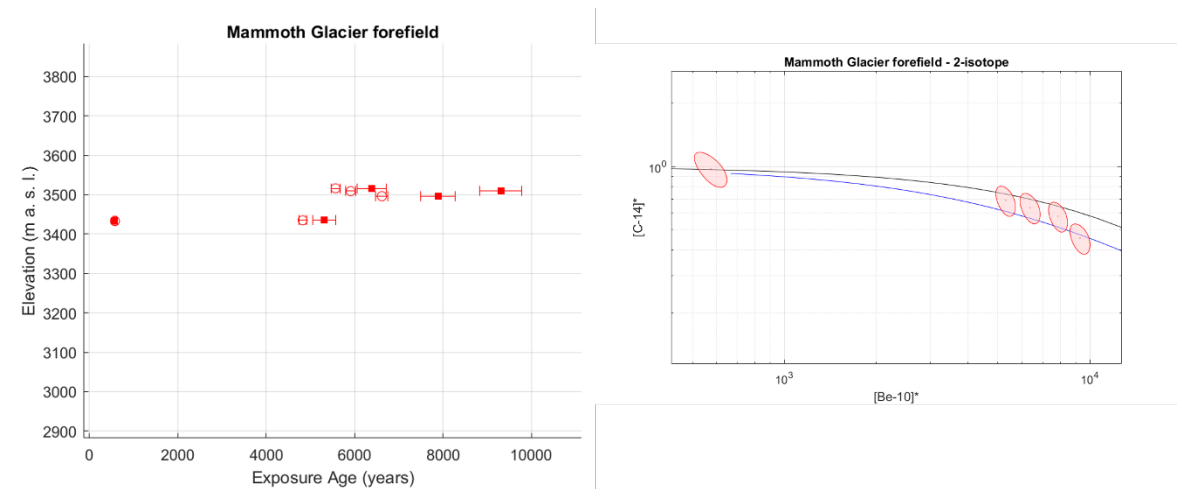


Site 25: Western upland nunatak, Sisimiut Peninsula (Greenland) – Type 1

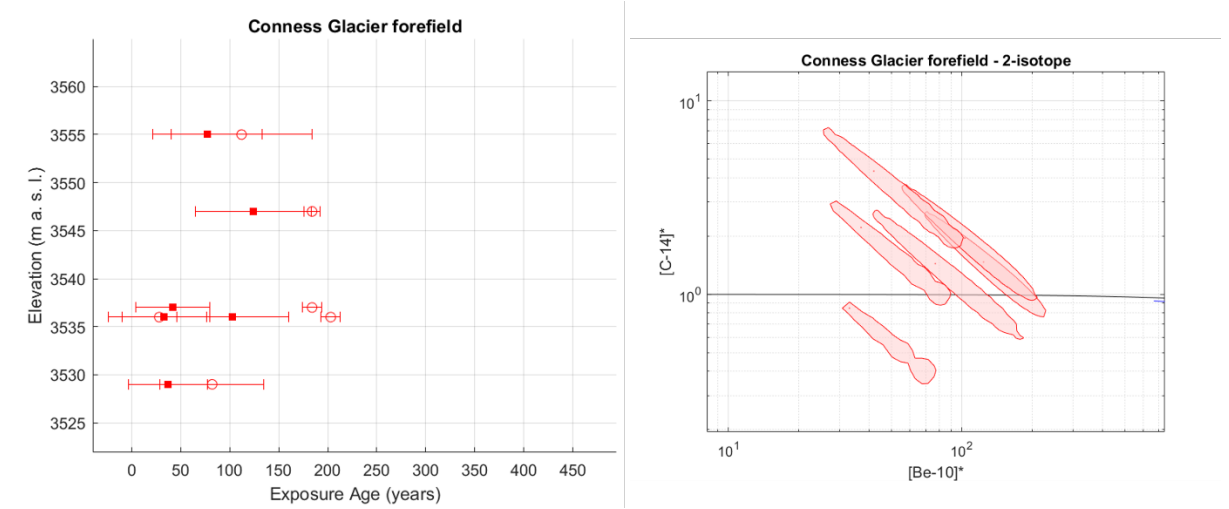


355

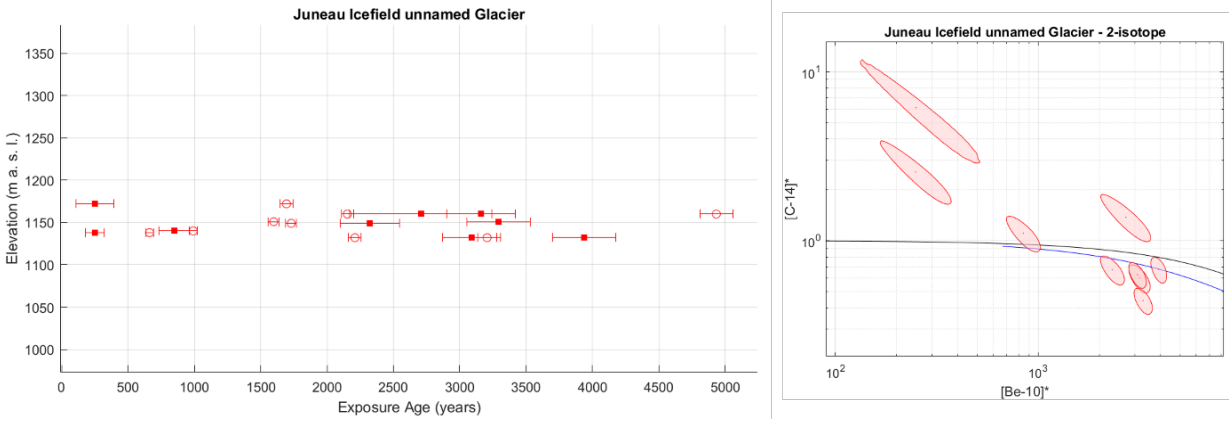
Site 26: Mammoth Glacier forefield, Wind River Range (Wyoming) – Type 1



360      **Site 27: Conness Glacier forefield, Sierra Nevada (California) – Type 1 2 3 (elongate)**



**Site 28: Unnamed Glacier, Juneau Ice Field (Alaska) – Type 1 2 3**



365

370

375

## **References – supplementary materials**

- 380 Adams, J. R., Johnson, J. S., Roberts, S. J., Mason, P. J., Nichols, K. A., Venturelli, R. A., Wilcken, K., Balco, G., Goehring, B., Hall, B., Woodward, J., and Rood, D. H.: New  $^{10}\text{Be}$  exposure ages improve Holocene ice sheet thinning history near the grounding line of Pope Glacier, Antarctica, *The Cryosphere*, 16, 4887–4905, <https://doi.org/10.5194/tc-16-4887-2022>, 2022.
- 385 Balco, G., Todd, C., Goehring, B. M., Moening-swanson, I., and Nichols, K.: Glacial geology and cosmogenic-nuclide exposure ages from the Tucker Glacier - Whitehall Glacier confluence, Northern Victoria Land, Antarctica, *American Journal of Science*, 319, 255–286, <https://doi.org/10.2475/04.2019.01>, 2019.
- 390 Balco, G., Brown, N., Nichols, K., Venturelli, R. A., Adams, J., Braddock, S., Campbell, S., Goehring, B., Johnson, J. S., Rood, D. H., Wilcken, K., Hall, B., and Woodward, J.: Reversible ice sheet thinning in the Amundsen Sea Embayment during the Late Holocene, *The Cryosphere*, 17, 1787–1801, 2023.
- Bevington, P. and Robinson, D.: *Data reduction and error analysis for the physical sciences*, edited by: Brufloft, D. and Cotkin, Spencer. J., McGraw Hill, New York, 1–313 pp., 1993.
- 395 Corbett, L. B., Bierman, P. R., Brown, T. A., Caffee, M. W., Fink, D., Freeman, S. P. H. T., Hidy, A. J., Rood, D. H., Wilcken, K. M., and Woodruff, T. E.: Clean quartz matters for cosmogenic nuclide analyses: An exploration of the importance of sample purity using the CRONUS-N reference material, *Quaternary Geochronology*, 73, 101403, <https://doi.org/10.1016/j.quageo.2022.101403>, 2022.
- 400 Fülöp, R.-H., Fink, D., Yang, B., Codilean, A. T., Smith, A., Wacker, L., Levchenko, V., and Dunai, T. J.: The ANSTO – University of Wollongong in-situ  $^{14}\text{C}$  extraction laboratory, *Nuclear Instruments and Methods in Physics Research Section B: Beam Interactions with Materials and Atoms*, 438, 207–213, <https://doi.org/10.1016/j.nimb.2018.04.018>, 2019.
- Johnson, J. S., Roberts, S. J., Rood, D. H., Pollard, D., Schaefer, J. M., Whitehouse, P. L., Ireland, L. C., Lamp, J. L., Goehring, B. M., Rand, C., and Smith, J. A.: Deglaciation of Pope Glacier implies widespread early Holocene ice sheet thinning in the Amundsen Sea sector of Antarctica, *Earth and Planetary Science Letters*, 548, 116–501, <https://doi.org/10.1016/j.epsl.2020.116501>, 2020.
- 405 Jull, A. J. T., Scott, E. M., and Bierman, P.: The CRONUS-Earth inter-comparison for cosmogenic isotope analysis, *Quaternary Geochronology*, 26, 3–10, <https://doi.org/10.1016/j.quageo.2013.09.003>, 2015.
- 410 Koester, A. J. and Lifton, N. A.: Technical note: A software framework for calculating compositionally dependent in situ  $^{14}\text{C}$  production rates, *Geochronology*, 5, 21–33, <https://doi.org/10.5194/gchron-5-21-2023>, 2023.
- Lifton, N., Sato, T., and Dunai, T. J.: Scaling in situ cosmogenic nuclide production rates using analytical approximations to atmospheric cosmic-ray fluxes, *Earth and Planetary Science Letters*, 386, 149–160, <https://doi.org/10.1016/j.epsl.2013.10.052>, 2014.
- 415 Milillo, P., Rignot, E., Rizzoli, P., Scheuchl, B., Mouginot, J., Bueso-Bello, J. L., Prats-Iraola, P., and Dini, L.: Rapid glacier retreat rates observed in West Antarctica, *Nature Geoscience*, 15, 48–53, <https://doi.org/10.1038/S41561-021-00877-Z>, 2022.
- Mouginot, J., Scheuchl, B., and Rignot, E.: Mapping of Ice Motion in Antarctica Using Synthetic-Aperture Radar Data, *Remote Sensing*, 4, 2753–2767, <https://doi.org/10.3390/rs4092753>, 2012.

- 420 Mouginit, J., Rignot, E., Scheuchl, B., and Millan, R.: Comprehensive annual ice sheet velocity mapping using Landsat-8, Sentinel-1, and RADARSAT-2 data, *Remote Sensing*, 9, 1–20, <https://doi.org/10.3390/rs9040364>, 2017.
- Nichols, K. A., Goehring, B. M., Balco, G., Johnson, J. S., Hein, A. S., and Todd, C.: New Last Glacial Maximum ice thickness constraints for the Weddell Sea Embayment, Antarctica, *The Cryosphere*, 13, 2935–2951, <https://doi.org/10.5194/tc-13-2935-2019>, 2019.
- 425 Rignot, E., Mouginit, J., and Scheuchl, B.: Antarctic grounding line mapping from differential satellite radar interferometry, *Geophysical Research Letters*, 38, 1–6, <https://doi.org/10.1029/2011GL047109>, 2011.
- 430 Simões Pereira, P., van de Flierdt, T., Hemming, S. R., Hammond, S. J., Kuhn, G., Brachfeld, S., Doherty, C., and Hillenbrand, C. D.: Geochemical fingerprints of glacially eroded bedrock from West Antarctica: Detrital thermochronology, radiogenic isotope systematics and trace element geochemistry in Late Holocene glacial-marine sediments, *Earth-Science Reviews*, 182, 204–232, <https://doi.org/10.1016/j.earscirev.2018.04.011>, 2018.